Available online at www.sciencedirect.com

ScienceDirect

International Journal of Solids and Structures 44 (2007) 1787–1808

INTERNATIONAL JOURNAL OF SOLIDS and STRUCTURES

www.elsevier.com/locate/ijsolstr

Void interaction and coalescence in polymeric materials

L. Cheng *, T.F. Guo

Department of Mechanical Engineering, National University of Singapore, BlK EA, 9 Engineering Drive 1, Singapore 117576, Singapore

Received 1 May 2006
Available online 10 August 2006

Communicated by Guest Editor T. Nakamura

Abstract

Beyond pressure-sensitivity, plastic deformation of glassy polymers exhibits intrinsic softening followed by progressive rehardening at large strains. This highly nonlinear stress–strain behavior is captured by a constitutive model introduced in this work. In the first part of the paper, we focus on void growth and coalescence in an axisymmetric representative material volume consisting of a single large void and a population of discrete microvoids. Our study shows that microvoid cavitation, enhanced by strain softening, accelerates the process of void coalescence resulting in brittle-like failure at lowered stresses and strains. Pressure-sensitivity also reduces stress-carrying capacity as well as influences the strain for void coalescence; plastic dilatancy effects are relatively milder. In the second part of the paper, we introduce a population of discrete spherical voids within a three-dimensional computational model to study void growth and damage ahead of a crack front. Our studies reveal a distinctive change in the deformed void shape from oblate to prolate when strain softening is followed by high rehardening at large plastic strains. By contrast, an extended strain softening regime promotes oblacity and facilitates multiple void interaction and their cooperative growth over large distances ahead of the crack front. This multi-void failure mechanism is exacerbated by pressure-sensitivity.

Keywords: Microvoids; Internal necking; Softening and rehardening; Pressure-sensitivity; Plastic dilatancy

1. Introduction

Various modifier particles are added to polymers to improve their mechanical properties, including fracture toughness. In such polymer systems, large voids can originate by cavitation of rubber particles in polymer-rubber blends or from decohesion of hard filler particles (Kim et al., 1996). In glassy and semicrystalline polymers, microvoids nucleate in zones of intense shearing – this appears to be related to the evolution of free volume, and possibly coalescence of free volume, in the strain softening regime (Hasan et al., 1993; Wright et al., 2003). Another damage mechanism called crazing entails microvoids growing in a well confined zone of highly

* Corresponding author. Tel.: +65 6874 6888/6516 6888; fax: +65 6779 1459.
E-mail address: MPECL@nus.edu.sg (L. Cheng).

0020-7683/$ - see front matter
doi:10.1016/j.ijsolstr.2006.08.007

stretched material perpendicularly oriented to the maximum principal tensile stress (Kramer and Berger, 1990). At the same time, it has been observed that large voids are likely initiation sites for shear bands and crazes, both of which involve the cooperative growth of many microvoids. In this work, we study the mechanical response and failure modes of glassy polymeric materials using a computational model encompassing two populations of cavities of different size-scales – large primary voids surrounded by many microvoids or micropores.

Compared to glassy polymers and polymer-rubber blends, there is a better understanding of the roles of primary voids and secondary microvoids on the mechanical response and fracture of metallic materials. The influence of void size and distribution on void growth, interaction and coalescence has been studied extensively for metals, e.g. Koplik and Needleman (1988) who employed a periodic array of identical voids. To gain some understanding of the interaction between primary voids and secondary microvoids, Faleskog and Shih (1997) introduced a representative material volume containing a single large void and a population of discrete microvoids. They observed that final rupture was dominated by a succession of rapidly growing microvoids, which involved the synergistic interaction between elasticity associated with high stress triaxiality and stiffness softening caused by plastic yielding. Tvergaard (1998) studied the interaction of very small voids with larger voids in metal matrix composites, and affirmed the importance of plastic flow localization in driving cavitation instability of very small voids. Perrin and Leblond (2000) examined the void growth arising from two populations of cavities of different size-scales in ductile metals. They showed that the existence of secondary microvoids played a pivotal role in material failure soon after the initiation of void coalescence.

This work builds on ideas and results for metallic materials. We study how the growth of large primary voids (e.g. those originating from cavitated rubber particles) and the cooperative growth of discrete microvoids affect the mechanical behavior and failure of glassy polymers and reinforced blends. In this regard, it is well known that the deformation of polymers differs considerably from that of metals in several important respects. A key feature peculiar to glassy polymers is the nonlinear stress–strain behavior that precedes the peak yield stress, followed by post-yield strain softening. The latter can be attributed to the evolution of the local free volume associated with certain metastable states. Beyond this regime, polymeric solids undergo strain rehardening, which is related to chain alignment and stretching of the entangled polymer network. Based on the physical ideas elucidated in Boyce et al. (1988) and Wu and Van der Giessen (1993), Anand and Gurtin (2003) developed a continuum theory for elasto-viscoplastic deformation of amorphous solids incorporating the local free-volume as an internal variable. Their model adopts the kinematic assumption that plastic flow is incompressible and irrotational.

Beyond the softening–rehardening yield characteristics described above, experimental studies have shown that plastic yielding of polymers is highly pressure-sensitive (e.g. Quinson et al., 1997). Some have observed that certain polymers exhibit modest levels of plastic dilatancy (e.g. G'Sell et al., 2002; Utz et al., 2004). Using a non-associated flow rule, Chew et al. (2006) conducted a numerical study of microvoid interaction in pressure-sensitive dilatant materials under proportional straining. They showed that increasing pressure-sensitivity severely reduces the materials' stress carrying capacity, while multiple void interactions were responsible for the sharp post-peak stress drop, triggering rapid failure.

This work explores how several distinctive characteristics of polymers – strain softening followed by rehardening, pressure-sensitivity and plastic dilatancy – affect void growth, void interaction and subsequent coalescence. Section 2 describes the constitutive model used for the polymeric matrix. The numerical procedure for the unit cell study is detailed in Section 3. Results for the single void cell study as well as the multiple void interaction study are presented in Section 4. In Section 5, the focus is on the effects of strain softening–rehardening and pressure-sensitivity on the damage evolution ahead of a crack. A short summary in Section 6 concludes this paper.

2. Modeling of a polymeric material

Polymers have complex, manifold deformation regimes. After undergoing relatively small amounts of plastic flow, they exhibit an intrinsic strain softening regime, followed by rehardening as straining progresses. Moreover, plastic yielding is pressure-dependent and plastic flow can be non-volume preserving. With these characteristics in mind, we present a simple phenomenological model for plastic flow in glassy polymers.

2.1. Pressure-sensitivity and dilatancy

The pressure-dependent yielding of polymers can be described by a yield criterion based on a linear combination of the mean stress σ_m and effective stress σ_e (Jeong et al., 1994; Chowdhury and Narasimhan, 2000). The pressure-dependent yield criterion is given by

$$\sigma_e + 3\alpha\sigma_m - \hat{\sigma} = 0 \tag{2.1}$$

where $\hat{\sigma}$ the flow stress of the subsequent yield surface. The pressure-sensitivity index α is related to the differential tensile and compressive yield stresses, as later defined in (2.6). It is also related to the friction angle ψ_α by $\tan\psi_\alpha = 3\alpha$. In polymeric materials, the typical friction angle ψ_α ranges between 0° and 23°.

We assume the flow potential to take the form

$$\Phi = \sigma_e + 3\beta\sigma_m \tag{2.2}$$

where β is the index for plastic dilatancy, which is related to the dilation angle ψ_β by $\tan\psi_\beta = 3\beta$. The Drucker–Prager yielding condition (2.1) together with the flow potential (2.2) can describe the pressure-sensitive dilatant behavior of the material. The plastic part of the deformation rate $\mathbf{d}^p$ is given by the flow rule

$$\mathbf{d}^p = \dot{\epsilon}^p \frac{\partial \Phi}{\partial \boldsymbol{\sigma}} \tag{2.3}$$

where $\dot{\epsilon}^p \equiv \sqrt{\frac{2}{3}\mathbf{e}^p : \mathbf{e}^p}$ is the equivalent strain rate, in which $\mathbf{e}^p$ is the deviatoric part of $\mathbf{d}^p$. The flow stress $\hat{\sigma}$ in (2.1) is a function of the accumulated plastic strain $\epsilon^p = \int \dot{\epsilon}^p \, dt$. For the case of $\beta = \alpha$, the normals to the yield surface (2.1) and the flow surface (2.2) in stress space coincide resulting in an associated plastic flow.

The utilization of an associated flow rule overstates the extent and role of plastic dilatancy (Subramanya et al., 2006). A non-associated flow, with $\beta < \alpha$, offers a more realistic description of plastic flow. In this paper more attention is given to an associated flow rule. The behavior of polymers exhibiting low plastic dilatancy, including vanishing dilatancy, will be taken up in a subsequent study.

2.2. Strain softening and rehardening

Glassy polymers display a true stress–strain curve exhibiting a maximum followed by a softening regime. As deformation proceeds further, they exhibit rehardening (related to chain alignment). In order to describe this post-yield behavior of polymers, we propose the flow stress model

$$\frac{\hat{\sigma}}{\sigma_0} = 1 + \frac{\epsilon^p}{\epsilon_0}\left(\frac{1}{1+\xi(\epsilon^p/\epsilon_0)^2} + \frac{\epsilon^p}{\eta}\right) \tag{2.4}$$

where ξ dictates the maximum, also called the intrinsic yield point, and η parameterizes the softening–rehardening shape of the stress–strain curve. The initial yield stress σ_0 (under shear) is related to the initial tensile and compressive yield stresses σ_0^t and σ_0^c, by

$$\sigma_0 = \begin{cases} (1+\alpha)\sigma_0^t & \text{for tension} \\ (1-\alpha)\sigma_0^c & \text{for compression} \end{cases} \tag{2.5}$$

The pressure-sensitivity index α in (2.1) can be determined by σ_0^t and σ_0^c as

$$\alpha = \frac{\sigma_0^c - \sigma_0^t}{\sigma_0^c + \sigma_0^t}. \tag{2.6}$$

A power-law (monotonically) hardening description of plastic flow is given by

$$\frac{\sigma_0}{E}\left(\frac{\hat{\sigma}}{\sigma_0}\right)^{1/N} - \frac{\hat{\sigma}}{E} = \epsilon^p \tag{2.7}$$

where N is the hardening exponent ranging from 0 to 1. Comparisons of model predictions based on (2.4) and (2.7) allow us to draw on well-known results for metallic materials.

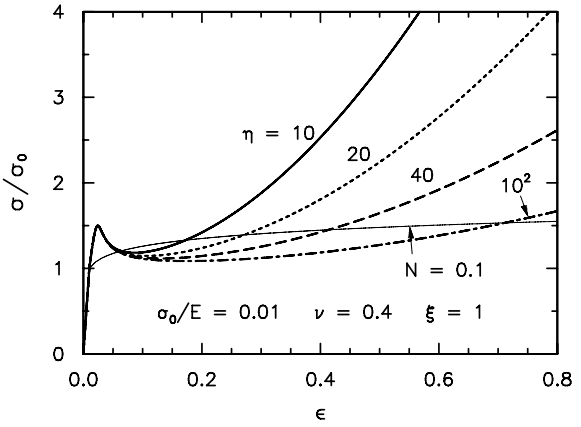

Fig. 1. Uniaxial true stress–strain relation for unvoided matrix. The intrinsic yield point and the rate of softening–rehardening are controlled by the parametric setting of $\xi = 1$ and $\eta = 10$, 20, 40, 100. A monotonically hardening relation (power-law with $N = 0.1$) is included for comparison.

The elastic response of the polymer is assumed to be linear and isotropic, with Young's modulus E and Poisson's ratio ν. With this definition, the reference strain, ϵ_0, is given by σ_0/E.

To help our understanding of the flow stress model (2.4), we describe the uniaxial response of the matrix (unvoided material) under the assumption of $\alpha = \beta = 0$. Fig. 1 depicts the uniaxial stress–strain curves for several η values with $\xi = 1$. When loaded beyond its initial yield stress σ_0, the material strain hardens and attains a maximum – the intrinsic yield stress. The increase of the intrinsic yield stress over and above σ_0 can be adjusted through the parameter ξ. As can be seen in Fig. 1, the parameter η is able to reproduce the three phases of polymer yielding observed experimentally – initial hardening, strain softening and then rehardening at large strains. Low η values (e.g. 10, 20, 40) simulate strain softening followed by high to moderate rehardening; high η values (e.g. 100) simulate an extended strain softening regime followed by low rehardening. For comparison, Fig. 1 also displays the stress–strain curve for a low monotonically hardening ($N = 0.1$) metal-like material.

The strain softening–rehardening characteristic of polymers can induce initiation and growth of shear bands. To illustrate this behavior, Fig. 2 contrasts the evolution of the accumulated plastic strain field ϵ^{p} around an isolated void (see the axisymmetric model described in Section 3) for two polymers, $\eta = 20$, 100, and a metal-like polymer, $N = 0.1$. The initial void size is given by $f_0 = 0.08$ and stress triaxiality $T = 2/3$ ($\Sigma_z = 4\Sigma_\rho$); the material parameters are shown in Fig. 1 (in this work, we fix $\xi = 1$). These simulations employ 4-node quadrilateral elements.

Fig. 2a displays the propagation of multiple shear bands in the polymer with $\eta = 20$. At the early stage of deformation $E_{\mathrm{e}} = 0.029$, we can detect two incipient shear bands near the equator. At $E_{\mathrm{e}} = 0.056$, a third band forms away from the equator. At higher deformation levels, plastic deformation is localized to the three inclined shear bands.

A similar trend is observed in Fig. 2b for the polymer described by $\eta = 100$. In this as well as in the previous case, the major shear bands have inclined angles of about 60° from the equatorial plane. By contrast, the plastic flow in a material with metal-like response ($N = 0.1$) is more diffused – see Fig. 2c.

2.3. Cavitation and void instability

We conclude this section with a cavitation study of a spherical cavity in a finitely deformed incompressible solid subjected to internal pressure p and externally applied radial stress σ_r^A. Guo and Cheng (2003) have shown that the radial equilibrium solution takes the form

$$\frac{\sigma_r^A + p}{\sigma_0} = \int_{\epsilon_1}^{\epsilon_2} \frac{H(\epsilon)\,\mathrm{d}\epsilon}{1 - \exp(-3\epsilon/2)}, \tag{2.8}$$

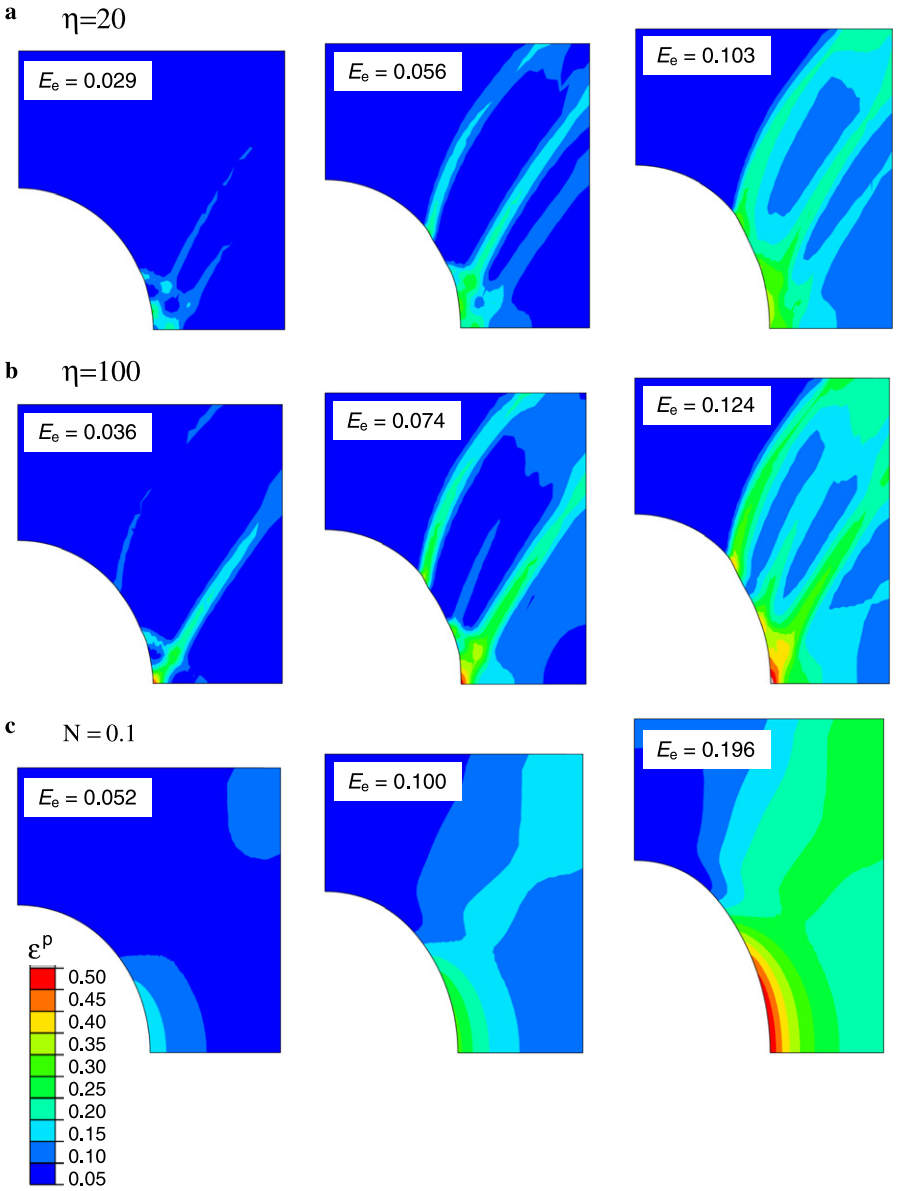

Fig. 2. Spatial distribution of accumulated plastic strain ϵ^p for several levels of macro-effective strain E_e for initial porosity $f_0 = 0.08$ and stress triaxiality $T = 2/3$. (a) $\eta = 20$; (b) $\eta = 100$; (c) $N = 0.1$.

where the uniaxial relationship between true stress and logarithmic strain of the material is described by $\sigma/\sigma_0 = H(\epsilon)$. The lower and upper integration limits ϵ_1 and ϵ_2 in (2.8) are the two-end strains of the void, which can be determined solely by the current and initial void volume fractions f and f_0

$$\epsilon_1 = \frac{2}{3}\ln\left(\frac{f_0}{f}\frac{1-f}{1-f_0}\right), \quad \epsilon_2 = \frac{2}{3}\ln\left(\frac{1-f}{1-f_0}\right). \tag{2.9}$$

In the pressure-insensitive case, $\alpha = \beta = 0$, the above radial solution is valid for the constitutive relations (2.4) and (2.7) since their elastic–plastic response can be written in the uniaxial stress–strain form $\sigma/\sigma_0 = H(\epsilon)$. For an elastic–plastic power-law hardening solid: $H(\epsilon) = \epsilon/\epsilon_0$ if $|\epsilon| < \epsilon_0$; otherwise $H(\epsilon) = (|\epsilon|/\epsilon_0)^N \mathrm{sign}(\epsilon)$. For an

Table 1
Critical stresses for spherically symmetric void growth

Hardening	Porosity, f_0	Critical stress, σ_c/σ_0		
		$\sigma_0/E = 0.01$	0.04	0.10
$\eta = 20$	0	6.93	3.67	2.54
	0.001	5.10	3.18	2.33
	0.01	3.34	2.61	2.03
	0.05	2.31	1.99	1.62
$\eta = 40$	0	5.54	3.34	2.43
	0.001	4.27	2.98	2.26
	0.01	3.16	2.53	1.99
	0.05	2.29	1.98	1.61
$\eta = 100$	0	4.61	3.12	2.35
	0.001	3.83	2.87	2.21
	0.01	3.08	2.49	1.97
	0.05	2.28	1.97	1.60
$N = 0.1$	0	4.22	2.90	2.14
	0.001	3.80	2.70	2.01
	0.01	3.05	2.31	1.77
	0.05	2.12	1.74	1.39

elastic–plastic, softening–rehardening solid, $H(\epsilon) = \epsilon/\epsilon_0$ if $|\epsilon| < \epsilon_0$, and $H(\epsilon)$ for $|\epsilon| \geqslant \epsilon_0$ can be determined from (2.4) by inserting $\epsilon^{\mathrm{p}} = \epsilon - \sigma/E = \epsilon - H\epsilon_0$.

For any non-vanishing initial porosity, the right-hand side of (2.8) has a peak value designated by σ_c/σ_0. That is, $\sigma_c = \max_f(\sigma_r^A + p)$ for a given f_0. This is the critical stress for unstable void growth. In the limiting case of $f_0 = 0$, σ_c is the so-called cavitation stress (Huang et al., 1991). Using the procedure outlined in Guo and Cheng (2003), we compute the cavitation and critical stresses for void growth in both types of solids. The values of σ_c/σ_0 for $\sigma_0/E = 0.01, 0.04, 0.1$; $f_0 = 0, 0.001, 0.01, 0.05$ are given in Table 1 for several η values and also for $N = 0.1$. It can be seen that the critical stresses for porous materials, $f_0 = 0.001, 0.01, 0.05$, are considerably lower than those for the void free material, $f_0 = 0$. For the case of $\eta = 20$, the cavitation stress for the material with large yield strain, $\sigma_0/E = 0.1$, is only about one third of that for $\sigma_0/E = 0.01$. Most polymers can sustain relatively large elastic strains before plastic yielding (compared to metals) and hence the cavitation stresses are significantly lower (Steenbrink and Van der Giessen, 1997a; Tvergaard, 1999).

3. Cell model and numerical implementation

In order to reproduce the experimentally observed failure behaviors of the dimple fracture in a low carbon steel and void sheet formation in AISI 4320 steel, Faleskog and Shih (1997) developed a plane strain cell model accounting for several modes of coalescence assisted by microvoid cavitation. The cell volume they employed contains one centrally-positioned large void and a number of discrete microvoids. All voids, modeled as cylindrical holes, are present from the very beginning of straining. Such an approach was also adopted by Chew et al. (2006) to study the multiple void interactions in pressure-sensitive solids.

Micrographs of modified polypropylenes (PP) obtained by Kim et al. (1996) showed that larger voids, originating from cavitation in rubber modified PPs or decohesion of alumina particles in PPs, are initiation sites for shear bands and crazes. Micrographs in G'Sell et al. (2002) revealed shear bands and crazes being formed in the shoulder of the neck in polyethylene terephtalate test samples. Motivated by the above studies, we adopt an axisymmetric geometry which accommodates two possible modes of void coalescence, akin to those operative in cup-cone fracture under axisymmetric tension (Tvergaard and Needleman, 1984).

3.1. Axisymmetric model

The representative material volume (RMV) consists of a periodic assemblage of hexagonal unit cells. Each unit cell has a large spherical void of radius r_0 at its center. To facilitate axisymmetric calculations, the

hexagonal cells can be approximated as cylindrical cells, each having an initial height $2L_0$ and radius R_0. The initial porosity of the large spherical void is given by

$$f_0 = \frac{2}{3}\frac{r_0^3}{R_0^2 L_0}.$$

Roller boundary conditions are applied along the symmetry planes of the quarter geometry of the cell volume to be analyzed (see example mesh in Fig. 3a). A cylindrical coordinate system with orthonormal frame $\{\mathbf{e}_\rho, \mathbf{e}_\phi, \mathbf{e}_z\}$ is adopted.

The contributions of secondary microvoids to the coalescence aspect of ductile fracture are studied via unit-cells that contain two populations of cavities of different size-scales. Similar to the single void cell in Fig. 3a, the larger cavity is located at the center of the cell, while the secondary microvoids are placed along the ligament (Fig. 3b) and along the diagonal of the cell (Fig. 3c). These are likely locations of cooperative microvoid

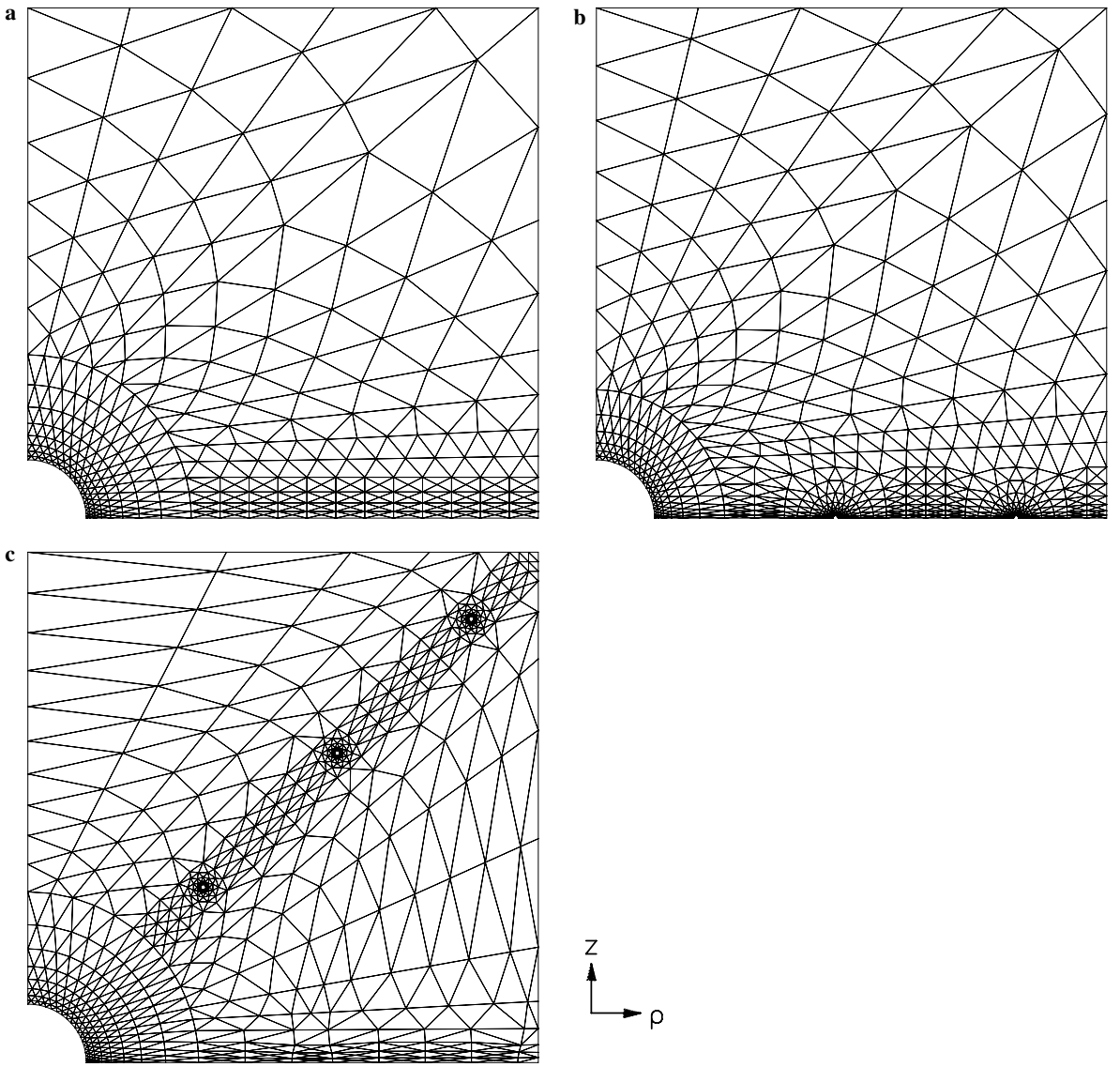

Fig. 3. Finite element meshes for three axisymmetric unit-cells where cylindrical coordinate system (z, ρ) is used, with z denoting the axis of revolution, and ρ the radial direction: (a) single void cell; (b) unit-cell with ligament microvoids; (c) unit-cell with diagonal microvoids.

growth resulting in the formation of crazes and shear bands which eventually link together the primary voids. Due to axial symmetry, each microvoid forms a ring torus within the cell. The microvoids are uniformly distributed with equal void spacing on the defined plane from the larger void. The radius of each microvoid is fixed at $r_0^m = 0.005L_0$.

In reality, unconnected cavitation sites are formed around the main cavity. Here the ring-like modeling of the secondary microvoids can be viewed as an idealized collective description of cavitation sites around the revolution axis of the axisymmetric geometry. A more realistic geometry, modeling discrete unconnected cavitation sites around the main cavity, is computationally challenging. It is a possible topic for future study.

The finite element mesh employs six-noded axisymmetric triangular elements. The computations are performed within the finite strain setting using the general purpose finite element program ABAQUS Version 6.5.1 (Hibbit et al., 2005). Computations are carried out under a prescribed stress triaxiality, using the numerical procedure presented in the section below.

3.2. Numerical procedure

For axisymmetric unit-cell studies, the macroscopic deformation gradient is given by

$$\bar{\mathbf{F}} = \lambda_\rho(\mathbf{e}_\rho \otimes \mathbf{e}_\rho + \mathbf{e}_\phi \otimes \mathbf{e}_\phi) + \lambda_z \mathbf{e}_z \otimes \mathbf{e}_z \tag{3.1}$$

where λ_ρ and λ_z are the principal stretches in the radial and axial directions, respectively. Eq. (3.1) specifies the macroscopic principal strains (E_ρ, E_z) and one effective strain measure E_e:

$$E_\rho = \ln \lambda_\rho, \quad E_z = \ln \lambda_z, \quad E_e = \frac{2}{3}|E_z - E_\rho|. \tag{3.2}$$

The work-conjugate stresses to (E_ρ, E_z) are the macroscopic Cauchy principal stresses (Σ_ρ, Σ_z). The macroscopic effective stress Σ_e and macroscopic mean stress Σ_m are given by $\Sigma_e = |\Sigma_z - \Sigma_\rho|$ and $\Sigma_m = \frac{1}{3}(\Sigma_z + 2\Sigma_\rho)$, which define the stress triaxiality $T = \Sigma_m/\Sigma_e$.

On the remote surfaces of $\rho = R_0$ and $z = L_0$, we impose the respective displacements

$$u_\rho = (\lambda_\rho - 1)\rho, \quad u_z = (\lambda_z - 1)z. \tag{3.3}$$

In rate forms, we have

$$\dot{u}_\rho = \dot{E}_\rho(u_\rho + \rho), \quad \dot{u}_z = \dot{E}_z(u_z + z), \tag{3.4}$$

where $\dot{E}_\rho = \dot{\lambda}_\rho/\lambda_\rho$ and $\dot{E}_z = \dot{\lambda}_z/\lambda_z$ are the macro principal strain rates. A prescribed stress triaxiality T is accomplished by keeping the stress ratio

$$\varphi = \Sigma_\rho/\Sigma_z \tag{3.5}$$

fixed during the analysis, where $T = (1 + 2\varphi)/(3(1 - \varphi))$ for axially dominant loading with $\Sigma_z > \Sigma_\rho$. This requirement on the stress ratio can be realized in a *multipoint constraint* of the displacement rates on the outer boundary.

The implementation of the above procedure is outlined in Appendix A. This procedure can also be applied to axisymmetric cells with a curved cell boundary such as spherical cells. Its small strain version has been used to compute the macroscopic yield surfaces for a thick spherical shell with pressure-sensitive matrices (Guo et al., in preparation).

4. Cell-model results

The properties of the polymeric material are specified by $\sigma_0/E = 0.01$, $\nu = 0.4$ with the softening–rehardening parameter η ranging from 10 to 100. The monotonically hardening power-law relation with $N = 0.1$ describes a metal-like stress–strain response. In this cell study we take $R_0 = L_0$.

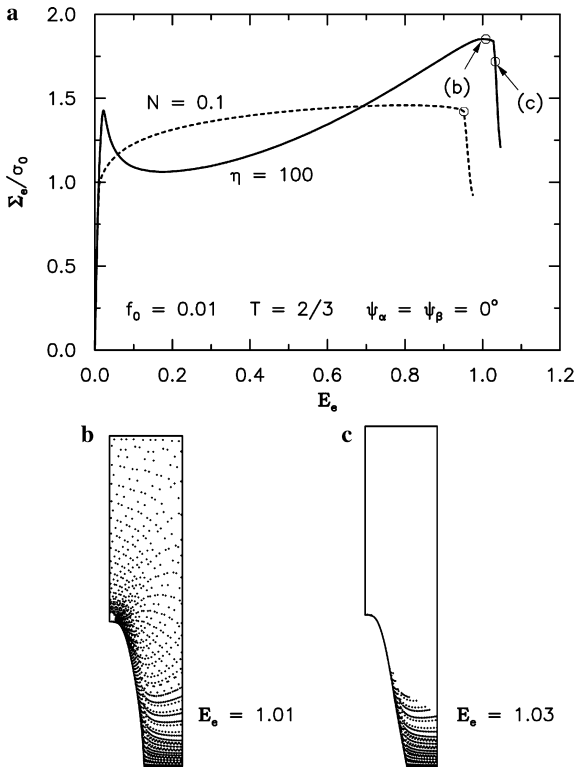

Fig. 4. Typical void coalescence behaviors for a single void cell. (a) Comparing macroscopic effective stress–strain response for softening–rehardening and monotonically hardening matrices. Active plastic zones for $\eta = 100$ in the current deformed configuration: (b) just before coalescence; (c) just after coalescence.

Void coalescence in porous ductile solids was studied numerically by Koplik and Needleman (1988). As a validation study, we first check this phenomenon for both hardening laws (2.4) and (2.7) in the case of $\alpha = \beta = 0$. Fig. 4a shows the macroscopic effective stress Σ_e versus effective strain E_e response for the single void cell under constant stress triaxiality $T = 2/3$ for $\eta = 100$ (solid line) and $N = 0.1$ (dotted line). Observe that for the metal-like material, $N = 0.1$, the macroscopic effective stress Σ_e increases gradually with effective strain E_e until a peak stress is reached. Beyond this point, Σ_e decreases smoothly as the rate of strain hardening is unable to compensate for the faster rate of (geometric) softening associated with void growth.

At effective strain $E_e = 0.95$, the sudden drop in the macroscopic effective stress indicates the onset of void coalescence. At this point (where rapid loss of Σ_e commences), the variation of the principal stretch in the radial direction λ_ρ with the effective strain E_e ceases to decrease. This marks the sudden shift in the macroscopic response of the cell to a uniaxial straining in the direction of the axis of symmetry. Following Koplik and Needleman (1988), the effective strain at this point is referred to as the critical effective strain E_c for the onset of void coalescence. The polymer characterized by $\eta = 100$ exhibits a similar behavior at the onset of coalescence even though the Σ_e–E_e curve displays a softening–rehardening behavior.

To corroborate the onset of void coalescence, the plastic states corresponding to the open circles labeled (b) and (c) in Fig. 4a are plotted in Fig. 4b and c, respectively. The active plastic zones, identified at the Gauss points, are shown in the current deformed configuration. One can see that the entire cell is fully-plastic prior to coalescence, $E_e = 1.01$. At a slightly larger effective strain, $E_e = 1.03$, the plastic deformation is localized around the ligament while the rest of the cell undergoes elastic unloading. This behavior is typical of the onset of void coalescence.

4.1. Single void results

Fig. 5 shows the single void response of a monotonically hardening material under three stress triaxiality levels $T = 2/3$, 1 and 2. Effects of pressure-sensitivity and plastic dilatancy on void coalescence are examined

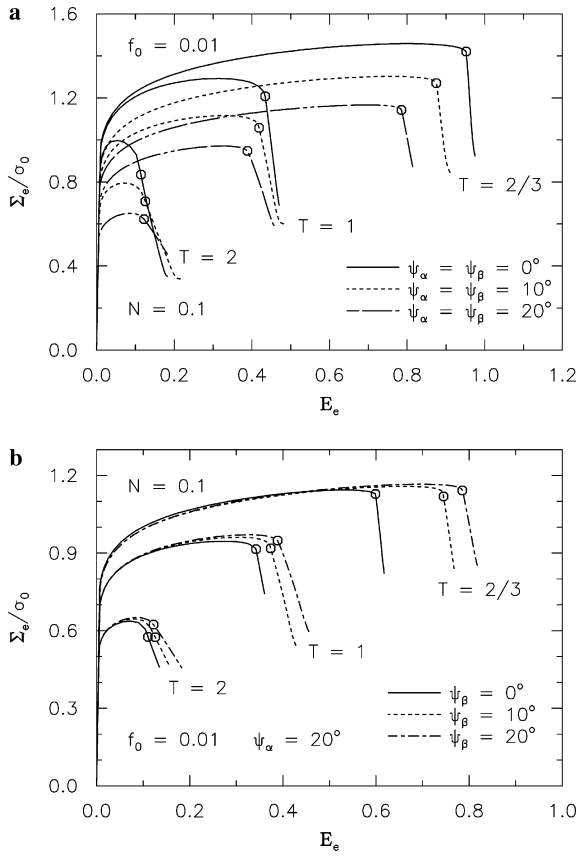

Fig. 5. Single void results for a monotonically hardening matrix with initial porosity $f_0 = 0.01$: (a) macro-effective stress–strain response under associated plastic flow and (b) non-associated plastic flow encompassing high and low dilatancy materials.

separately in Fig. 5a and b for the two cases: high dilatancy plastic flow $\alpha = \beta$, and lower dilatancy plastic flow $\beta < \alpha$.

In Fig. 5a, curves for pressure-insensitive plastic deformation ($\alpha = \beta = 0$) provide comparison curves for pressure-sensitive plastic behavior, $\psi_\alpha = \psi_\beta = 10°$, 20°. Observe that under a given stress triaxiality, the peak levels of the macroscopic effective stress Σ_e decrease proportionately with the increase of pressure-sensitivity and dilatancy. The corresponding effective strains at coalescence (indicated by open circles) also decrease, particularly for the lower stress triaxiality, $T = 2/3$. Pressure-sensitivity and plastic dilatancy lower the stress carrying capacity of the cell, contributing to more brittle-like behavior.

In Fig. 5b, the pressure-sensitivity is fixed at $\psi_\alpha = 20°$. This value is representative of a typical polymer such as PMMA (Quinson et al., 1997). The cases, $\psi_\beta = 0°$ and 10°, represent non-dilatant and moderately dilatant plastic flow. To facilitate comparison, the curves for $\psi_\beta = 20°$ (associated plastic flow) are included. The effect of plastic dilatancy on Σ_e is small prior to reaching the peak stress level. However plastic dilatancy has some influence on the critical effective strain for coalescence, E_c, especially at low stress triaxiality (see open circles for $T = 2/3$ in Fig. 5b). Putting aside the highest stress triaxiality case (where the trend is unclear), the value of E_c decreases with decreasing plastic dilatancy; E_c is lowest for non-dilatant plastic flow. This phenomenon could be attributed to the competition between matrix strain hardening and porosity induced softening. It could be argued that high plastic dilatancy of the matrix suppresses void growth thereby retarding void coalescence. Relative to the comparison curves, $\psi_\alpha = \psi_\beta = 20°$, low levels of plastic dilatancy leads to lower values of E_c as well as slight reduction in the stress carrying capacity. While the results in Fig. 5b indicate that plastic dilatancy effects are small relative to pressure-sensitivity effects, it suggests that ductility and fracture analyses based on an associated flow (plastic dilatancy is commensurate with pressure-sensitivity) could be slightly non-

conservative. Void growth and coalescence under low dilatancy plastic flow will be taken up in a subsequent work. In the remaining sections, attention will be directed to associated plastic flow ($\beta = \alpha$).

For the two stress–strain laws (2.4) and (2.7), it is of interest to compare their single void cell's response under several prescribed stress triaxialities. To this end, we choose $\eta = 20$ for the softening–rehardening material and $N = 0.1$ for the monotonically hardening material. Fig. 6a compares the macroscopic effective stress–strain curves for three triaxiality levels, $T = 2/3$, 1 and 2 ($\psi_\alpha = \psi_\beta = 0°$). Related to the progressive rehardening that follows strain softening, both E_c and the peak Σ_e for $\eta = 20$ are significantly larger than their counterparts for $N = 0.1$ (compare the open circles with triangles in Fig. 6a). For $T = 1$, the critical effective strain for coalescence for $\eta = 20$ is about 3 times larger than that for $N = 0.1$. For both material types, E_c decreases as the triaxiality increases.

Fig. 6b plots the evolution of void volume fraction f. It is of interest that f at the onset of coalescence, denoted by f_c, displays opposite trends for the two material types. As the stress triaxialities decrease from $T = 2$ to $T = 2/3$, the critical f values increase slightly for the metal-like polymer, $N = 0.1$. By contrast the f_c values for the polymer with $\eta = 20$ decrease considerably. A closer examination of the void evolution plots indicate that initial void growth is larger for $\eta = 20$. As the straining continues, the $N = 0.1$ case grows faster, reaching coalescence earlier. The opposite trends appear to be related to the different post-yield characteristics of the two types of materials (see Fig. 1). We'll revisit these aspects in a subsequent section.

4.2. Microvoid-assisted void growth and coalescence

In this section, we study how microvoid cavitation along the ligament (Fig. 3b) and the diagonal (Fig. 3c) of the cell can assist the onset of coalescence. Results for the single void cell are also included for the purpose of comparison. The initial porosity of the primary void is set to $f_0 = 0.001$ for all the three cells.

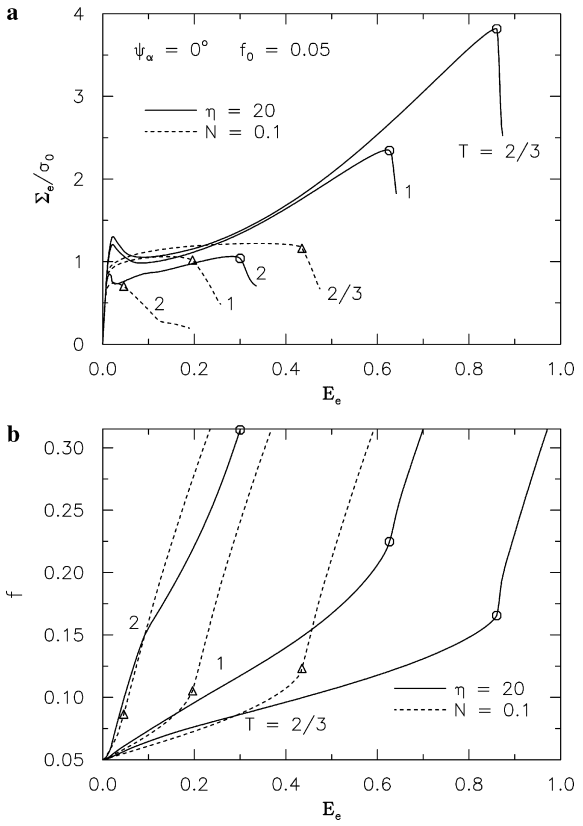

Fig. 6. Comparison of single void behavior for two types of stress–strain laws with $\psi_\alpha = \psi_\beta = 0°$ and $f_0 = 0.05$: (a) macro-effective stress–strain response and (b) void volume fraction vs. macro-effective strain.

4.2.1. Monotonically hardening material

First, we direct attention to the behavior of pressure-insensitive monotonically hardening materials. Fig. 7a shows the effect of microvoid interacting with the primary void. Under low stress triaxiality $T = 1$, the presence of ligament microvoids dramatically reduces the strain levels at onset of coalescence (compared to the single void cell). It is noteworthy that even at modest effective strain levels, the stress triaxiality near the ligament microvoids is high enough to induce cavitation, facilitating the coalescence process. At higher strain levels, the local stress triaxiality near the diagonal microvoids reaches levels sufficient to trigger microvoid cavitation, which assists shear banding. Under high stress triaxiality loading, $T = 2$, we observe that void coalescence for all three RMVs occur at much lower values of E_c; these values also fall within a narrower range of strains.

The simulations displayed in Fig. 7a suggest that ligament microvoids significantly accelerates the onset of coalescence under all stress triaxiality levels. This being the more critical case, we will use the unit-cell with ligament microvoids to study the effects of pressure-sensitivity α on the macroscopic stress–strain response under three stress triaxialities.

Fig. 7b shows the effective stress–strain response for the multi-void cell (containing a primary void and several ligament microvoids) under three different stress triaxiality levels and for three levels of pressure-sensitivity. Observe that an increase in pressure-sensitivity consistently lowers Σ_e across all triaxiality levels. We further note that α has some influence on the effective strain at the onset of coalescence, indicated by open circles in Fig. 7b. At low triaxiality level, $T = 1$, an increase in α from 0° to 20° can cause a noticeable reduction in E_c; this trend is reversed under high stress triaxiality level, $T = 2$.

Fig. 8 displays the deformed geometries for all the three unit-cells at the onset of coalescence, corresponding to the three cases in Fig. 7a for $T = 1$, with $\psi_\alpha = 0°$. In the absence of microvoids (see Fig. 8a), the cell deforms

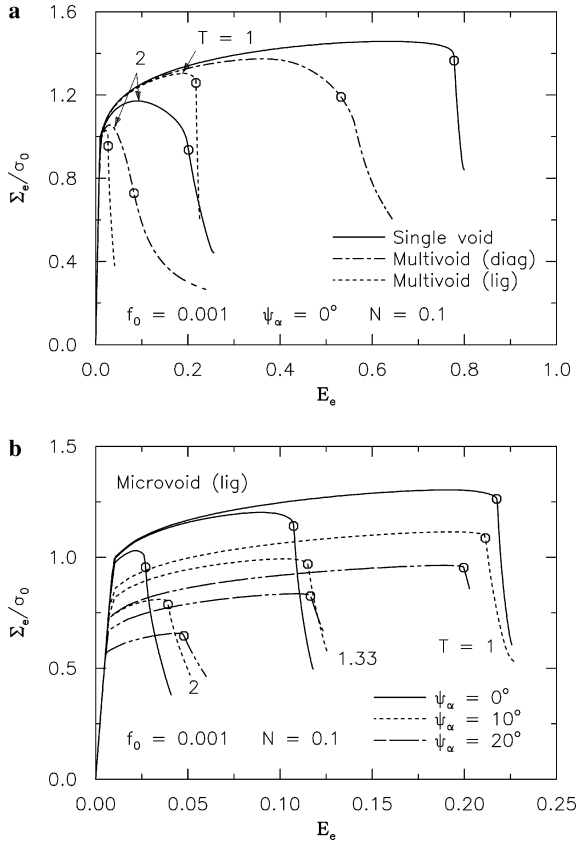

Fig. 7. Microvoid effects on coalescence in monotonically hardening matrix with initial porosity $f_0 = 0.001$: (a) pressure-insensitive yielding and (b) pressure-sensitive yielding.

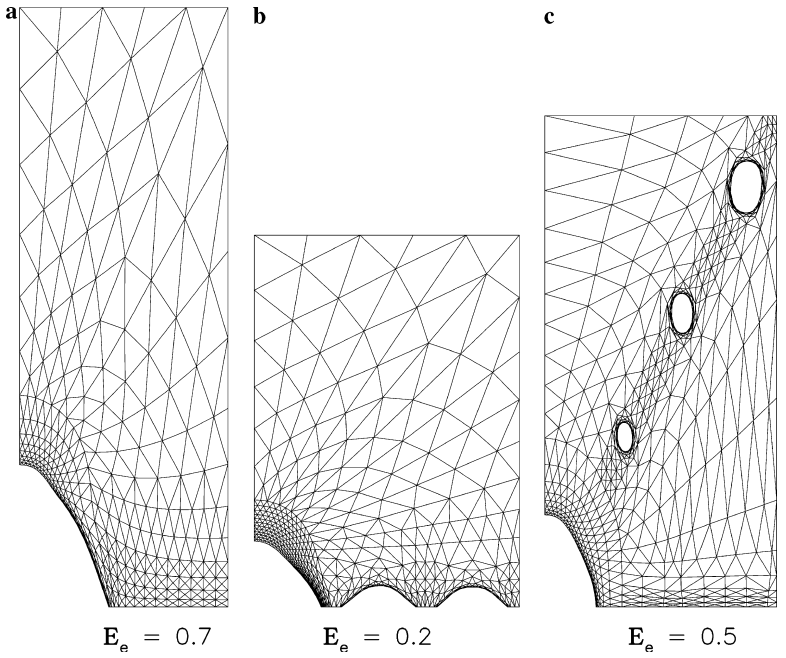

Fig. 8. Deformed meshes for monotonically hardening matrix, $N = 0.1$, near onset of coalescence: (a) single void cell; (b) multiple void cell with ligament microvoids and (c) multiple void cell with diagonal microvoids.

to a very large strain level, before the onset of failure via internal necking. When microvoids are present at the ligament (see Fig. 8b), the microvoid closest to the main cavity experiences cavitation instability and grows to several times its initial void size. The next closest microvoid then undergoes rapid void growth, which in turn drives the cavitation of its neighboring microvoid. This synergistic void growth process causes the cell to fail at much lower strain levels. For the cell containing diagonal microvoids (see Fig. 8c), the build up of stress triaxiality in the region diagonally midway between the two large voids causes the microvoids there to grow. This in turn drives up the triaxiality level between the newly enlarged microvoid and the main cavity, causing an in-between microvoid to cavitate. This sequence of events leads to void-by-void link-up. The above phenomena are discussed in greater detail by Faleskog and Shih (1997).

4.2.2. Strain softening and rehardening

With respect to the present unit cell geometry and loading, it appears that ligament microvoids has a more critical role in triggering coalescence. Hence we use the unit-cell with ligament microvoids to study the softening–rehardening effect (represented by η) on microvoid-assisted void growth and coalescence under low stress triaxiality, $T = 1$.

Fig. 9a focusses attention on the pressure-insensitive case, $\psi_\alpha = 0°$. For η ranging from 10 to 100, the ligament microvoid results (solid line) are plotted against the corresponding single void results (dotted line). It can be seen that the cavitated microvoids along the ligament greatly reduces the critical strain E_c for void coalescence, indicated by the open circles. The reduction is larger with increasing values of η. For $\eta = 100$, the critical strain E_c for the multiple void cell is only about one-fifth of that for the single void cell.

Fig. 9b displays the added effect of pressure-sensitivity, $\psi_\alpha = 0°$, 10°, 20°, for $\eta = 20$, 40 and 100. A careful study of the plots shows that pressure-sensitivity effects on ductility can be beneficial or detrimental. For polymers with sufficiently high rehardening, $\eta = 20$ and 40, the critical strain E_c for coalescence increases monotonically as ψ_α increases from 0° to 20°. However, an opposite effect is observed for a low rehardening material, $\eta = 100$. The latter behavior is similar to that seen in Fig. 7b for a low monotonically hardening solid, $N = 0.1$.

Fig. 10 shows the deformed meshes near the onset of coalescence for rehardening levels $\eta = 20$, 40, 100, with $\psi_\alpha = 0°$. Void shapes for secondary microvoids are more prolate as η decreases, indicating that high rehardening reduces void interaction effects. Void shapes for the primary voids also show a similar trend with

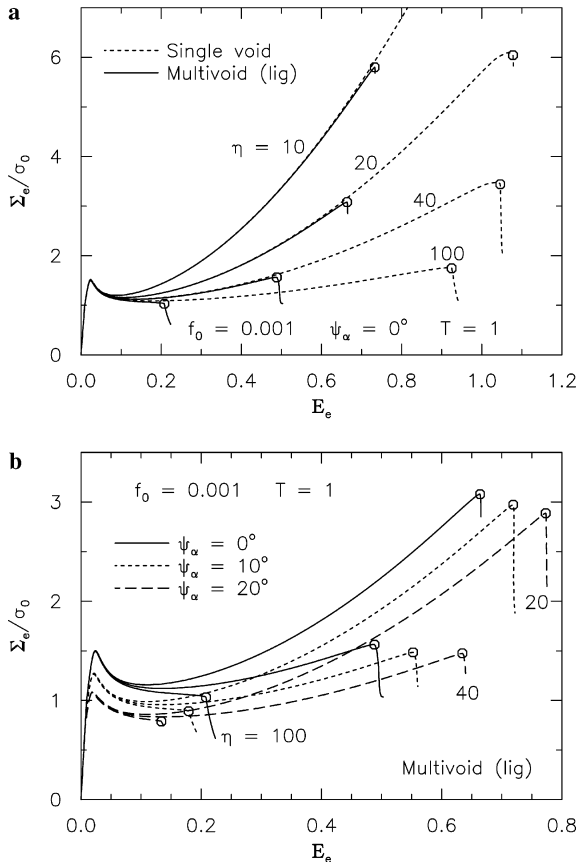

Fig. 9. Microvoid effects on coalescence for a softening–rehardening matrix with $f_0 = 0.001$: (a) $\eta = 10$, 20, 40, 100; pressure-insensitive yielding and (b) $\eta = 20$, 40, 100; pressure-sensitive yielding.

respect to η. Fig. 10a, however, deserves a further comment. The stress–strain curve for $\eta = 100$ (see Fig. 1) encompasses an extended softening regime followed by low rate of rehardening. A related effect is that the primary void deforms mainly around the neighborhood of the equator. The deformed void shape resembles to some extent the simulation by Steenbrink and Van der Giessen (1997b) (see Fig. 6 therein) using a more elaborate constitutive model for polymers. In this regard, it is noted that void shapes for low monotonically hardening solid, $N = 0.1$, are also more oblate (see Fig. 8b).

It is noteworthy that the primary void as well as the microvoids shown in both Figs. 8b and 10a (for similar RMVs) develop oblate shapes, notwithstanding the low stress triaxiality loading. These shapes suggests that cooperative growth and interaction between voids control the stress bearing capacity and ductility for the cases considered in this section.

5. Void interaction ahead of a crack

To study the growth and interaction of voids ahead of a crack, the fracture process zone has been modeled by a single row of discrete voids (Tvergaard and Hutchinson, 2002; Kim et al., 2003). This discrete model can be motivated by the computational cell approach proposed by Xia and Shih (1995a,b) and Xia et al. (1995). They simplified the ductile fracture process by placing a single row of void-containing elements ahead of the crack tip; this layer of computational cells was deemed to be representative of the fracture process zone. The behavior of the void-containing elements was governed by the constitutive laws of Gurson (1977). The computational cell approach was recently used to model the vapor pressure assisted void growth and rupture of electronic packages via an extended Gurson model (Cheng and Guo, 2003; Chew et al., 2005; Guo and Cheng, 2002, 2003).

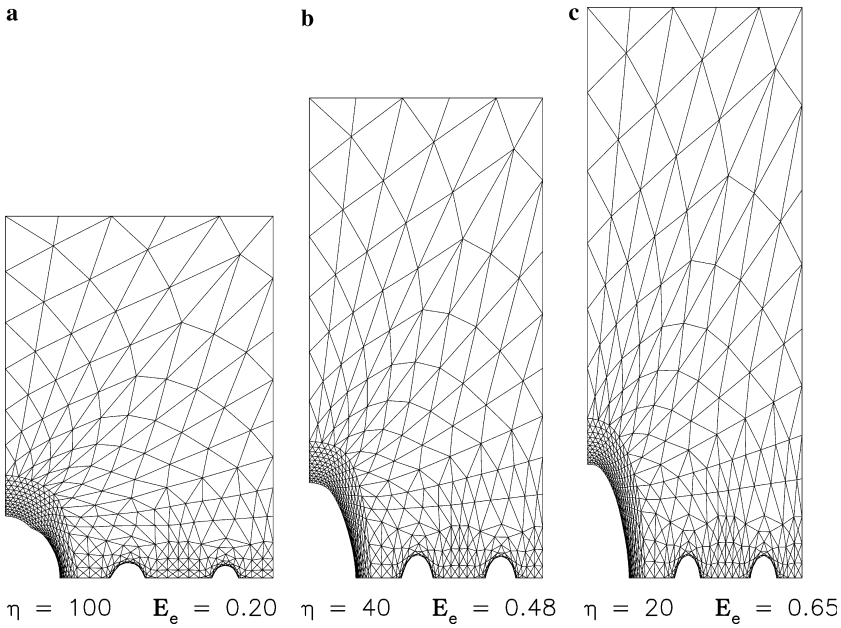

Fig. 10. Deformed meshes of the unit-cell with ligament microvoids for softening–rehardening matrix near onset of coalescence: (a) $\eta = 100$, $E_e = 0.20$; (b) $\eta = 40$, $E_e = 0.48$; and (c) $\eta = 20$, $E_e = 0.65$.

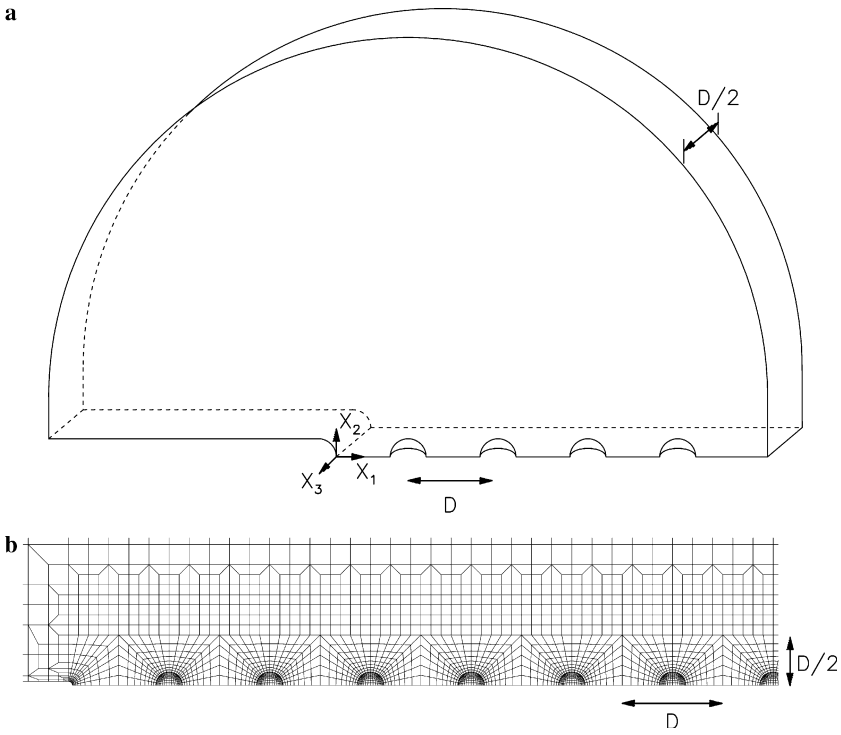

Fig. 11. (a) Slice of a cracked body showing periodic distribution of 3-D discrete voids ahead of the crack front. (b) Close-up view of initial mesh and discrete voids ($f_0 = 0.01$). A single row of 23 initially spherical voids, with spacing D, is placed ahead of the crack front.

5.1. 3-D discrete void model

We examine the multiple void interaction and growth ahead of a Mode I crack, paying particular attention to polymers exhibiting strain softening and rehardening (see Fig. 1). Fig. 11 displays the three-dimensional finite element model of a slice of a cracked body. A planar array of voids is placed on the ligament of the crack – discrete spherical voids with periodicity D by D in the X_1–X_3 plane,

By taking advantage of symmetry with respect to the crack plane, only the upper half of the slice needs to be modeled. Moreover, the deformation in the specimen thickness direction is assumed to be periodically symmetric with periodicity D. As such, only one-half of the (periodic) distance in the X_3-direction is modeled. Fig. 11a shows the upper half of the sliced body of thickness $D/2$. With respect to the slice being displayed, the ligament is modeled by a single row of cubic cells whose edges are subjected to plane strain conditions – displacement component $u_3 = 0$ at the planes $X_3 = 0$ and $X_3 = -D/2$. A close-up view of the ligament comprising cubic cells is provided in Fig. 11b.

The crack tip has a small initial root radius r_0, with the distance between the crack tip and nearest void fixed at D. Previous studies have shown the influence of r_0 to be negligible should the ratio of r_0/D be small. Here, we fix r_0 as $0.04D$. In summary, the slice encompasses a ligament which comprises 23 discrete cubic cells each containing a spherical void.

The unit-cell has dimensions $D \times D \times D$, and contains a discrete spherical void of initial radius R_0. The initial void volume fraction is defined by $f_0 = \frac{4}{3}\pi R_0^3/D^3$. The macroscopic stress of each unit-cell is computed from

$$\Sigma_{ij} = \frac{1}{V}\int_V \sigma_{ij}\,\mathrm{d}V \tag{5.1}$$

where σ_{ij} represents the local Cauchy stress within a voided cell, and V is the cell volume in the current deformed configuration. The macroscopic mean stress is given by $\Sigma_{\mathrm{m}} = \Sigma_{kk}/3$. The current void volume fraction is calculated from $f = V_f/V$ where V_f represents the current deformed void volume obtained by numerical integration.

5.2. Small-scale yielding

The boundary layer configuration for small scale yielding is depicted in Fig. 11a. Along the remote circular boundary of the slice, $R = 4000D$, we apply the asymptotic (in-plane) displacement field

$$\begin{aligned} u_1(R,\theta) &= K_{\mathrm{I}}\tfrac{1+\nu}{E}\sqrt{\tfrac{R}{2\pi}}(3-4\nu-\cos\theta)\cos\tfrac{\theta}{2} \\ u_2(R,\theta) &= K_{\mathrm{I}}\tfrac{1+\nu}{E}\sqrt{\tfrac{R}{2\pi}}(3-4\nu-\cos\theta)\sin\tfrac{\theta}{2} \end{aligned} \tag{5.2}$$

where $R^2 = X_1^2 + X_2^2$ and $\theta = \tan^{-1}(X_2/X_1)$ for points on the remote boundary. The mode I stress intensity factor K_{I} is related to the J-integral by

$$J = \frac{1-\nu^2}{E}K_{\mathrm{I}}^2. \tag{5.3}$$

At various stages of the loading, the value of the J-integral is calculated on a number of contours around the crack using the domain integral method (Moran and Shih, 1987). The domain integral value was found to be in good agreement with the value given by (5.3) for the prescribed amplitude K_{I}. This consistency check assures that small-scale yielding conditions are satisfied.

5.3. Results and discussion

From dimensional considerations, the spatial distribution X_1/D of the field quantities $\Sigma_{\mathrm{m}}/\sigma_0$ and f depends on the following dimensionless geometric-material parameters:

$$\frac{J}{\sigma_0 D};\quad \frac{\sigma_0}{E}, \nu, \alpha, \beta;\quad \xi, \eta \text{ (or } N);\quad f_0 \tag{5.4}$$

The material parameters are assigned these values: $\sigma_0/E = 0.01$, $\nu = 0.4$, $\xi = 1$ and $\beta = \alpha$. Our parametric study focusses on two values of the rehardening parameter η and two levels of pressure-sensitivity α.

Tvergaard and Hutchinson (2002) introduced a population of discrete cylindrical voids ahead of a plane strain crack to study two mechanisms of crack initiation and growth: (i) void by void growth mechanism and (ii) multiple void interaction-growth mechanism. The transition between these two mechanisms is primarily governed by the initial void porosity. At low porosities, f_0 less than about 0.001, the nearest void interacts with the crack tip resulting in void by void advance of the tip. The second mechanism, operative for large holes, involves the simultaneous interaction and growth of multiple voids ahead of the crack tip. The above observations were supported by a more detailed 3-D model in which spherical voids were placed ahead of a crack front (Kim et al., 2003). Compared to metals, modified polymers could be regarded as highly porous solids, e.g. cavitated rubber blends, with f_0 greater than about 0.01. The studies reported in this section employ two representative initial porosities, $f_0 = 0.01$, 0.05.

Attention is first directed to the evolving damage process zone for $f_0 = 0.01$ with plastic flow taken to be pressure-insensitive, $\alpha = 0$. To facilitate comparisons of damage mechanism evolution in different material types, the applied load J is monotonically increased until the near-tip void (the void adjacent to the crack) reaches the current void volume fraction $f_{\text{tip}} = 0.2$. This requirement can also be considered as the fracture initiation criterion.

Fig. 12 shows the spatial distribution of porosity f and mean stress Σ_m/σ_0 in the damage process zone for three materials: $N = 0.1$, and $\eta = 40$, 100. Multiple void interactions are observed in all three cases, encom-

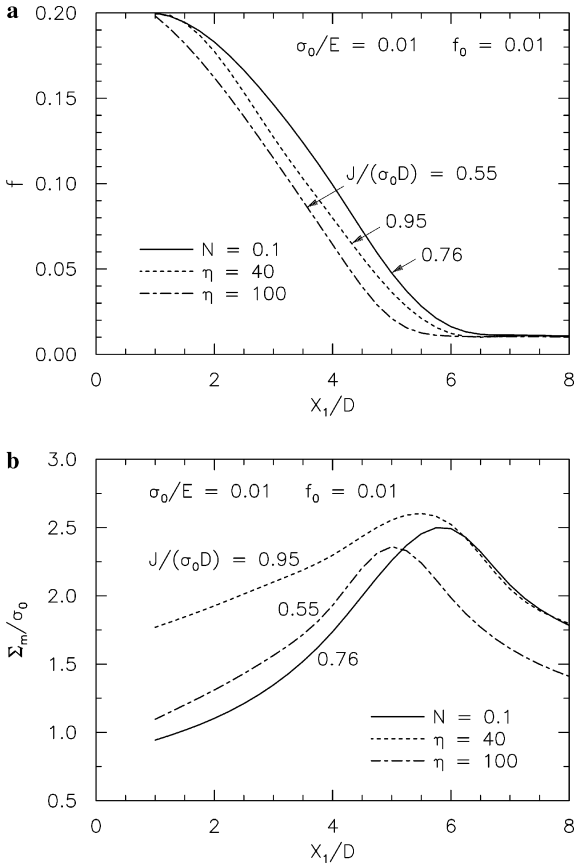

Fig. 12. Distribution of porosity f and mean stress Σ_m/σ_0 in the damage process zone when the void closest to the tip reaches porosity 0.2; $\sigma_0/E = 0.01$, $\nu = 0.4$, $\alpha = 0$, $f_0 = 0.01$.

passing a zone of 7 discrete voids. While the porosity distributions for the three materials differ only slightly, the stress distributions display larger variations. Within the damage process zone, the stress distribution for $N = 0.1$ is closer to that for $\eta = 100$; beyond the process zone it is closer to that for $\eta = 40$. In connection with the fracture initiation criterion, the critical load for $\eta = 40$ is largest, with $J/(\sigma_0 D) = 0.95$.

Fig. 13 displays the deformed meshes associated with the critical loads in Fig. 12, for $N = 0.1$, and $\eta = 40$ and 100. Though the near tip porosities have identical values ($f_{tip} = 0.2$), the three near-tip voids deform in different patterns. For the $\eta = 40$ material, the deformed void shape is prolate relative to the symmetry plane-(X_1, X_3). For $\eta = 100$, the deformed void shape is highly oblate. The deformed void shape for $N = 0.1$ exhibits highly non-uniform distortion, though it more closely resembles that for $\eta = 100$.

A close examination of the crack tips reveals different crack tip profiles. The smoothly blunted crack tip in Fig. 13a, for the monotonically hardening material, $N = 0.1$, agrees what had been widely reported in numerical studies for metals. For the strain softening–rehardening solids, $\eta = 40$, 100, the profiles in Fig. 13b and c suggest the initiation of superblunting – the early stage of circumferential cold-draw near the crack tip. This feature could be significant since superblunting along plane strain predominant crack tip segment was experimentally reported for modified polyproplene and numerically simulated using continuum damage mechanics models (Yang et al., 1993; Guo and Yang, 1993).

The results for $f_0 = 0.05$ are taken up next. Fig. 14 compares pressure-sensitivity effects, $\psi_\alpha = 10°$, on the damage distribution ahead of the crack for three levels of strain rehardening: $\eta = 20$, 40, 100. The results for $\psi_\alpha = 0°$ (solid line) are included for comparison purposes. Results show that a moderate level of pressure-sensitivity, $\psi_\alpha = 10°$, significantly increases the extent of the damage zone involving multiple void growth and interaction. In this case, the process zone engulfs at least two additional voids. Also note that under the same load of $J/(\sigma_0 D) = 0.35$, voiding activity ahead of the crack becomes increasingly stronger as η increases.

Fig. 15 shows the deformed voids ahead of the crack tip for $\eta = 20$, 100. As could be expected, void growth is more extensive for the $\eta = 100$ material. In particular, the voiding pattern – the enlarged size and the oblate shape of the voids – indicates high level of void growth and interaction extending over many voids ahead of

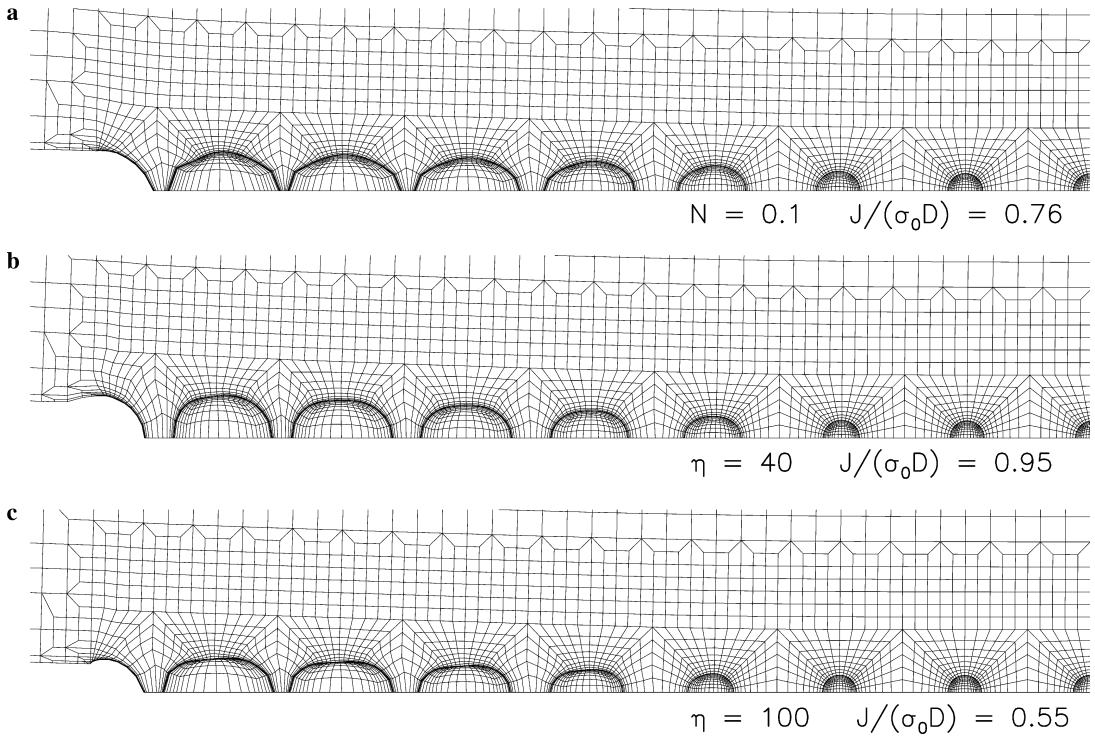

Fig. 13. Deformed meshes when the void closest to the tip reaches porosity 0.2. (a) $N = 0.1$ and $J/(\sigma_0 D) = 0.76$; (b) $\eta = 40$ and $J/(\sigma_0 D) = 0.95$ and (c) $\eta = 100$ and $J/(\sigma_0 D) = 0.55$.

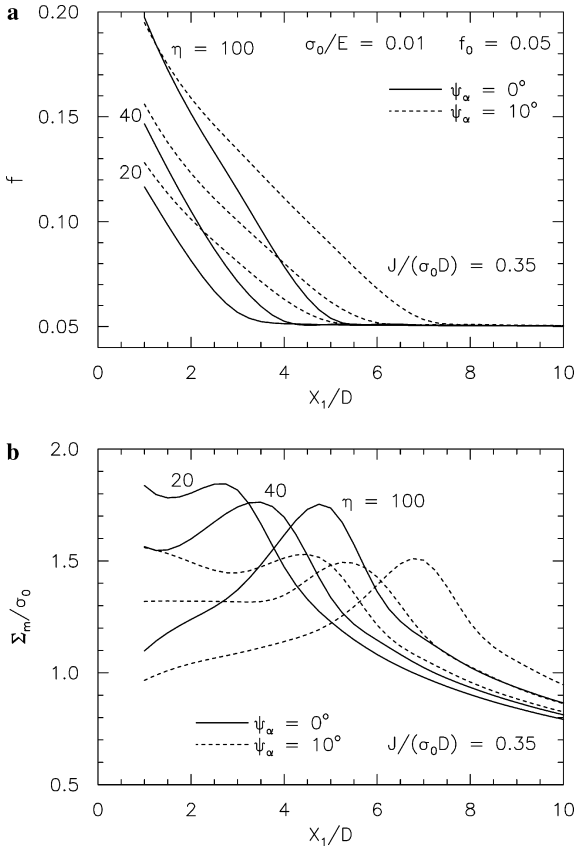

Fig. 14. Distribution of porosity f and mean stress Σ_m/σ_0 in the damage process zone for three softening–rehardening levels under applied load $J/(\sigma_0 D) = 0.35$; $\sigma_0/E = 0.01$, $\nu = 0.4$, $f_0 = 0.05$.

the crack tip. Such a multiple void interaction-growth mechanism determines the material's fracture resistance. This could also be inferred by using a void coalescence criterion based on the void reaching a critical size (as employed in relation to Fig. 12), or coalescence criterion based on the ligament between voids being reduced to a certain fraction of the initial void spacing as proposed by Tvergaard and Hutchinson (2002) – compare their Fig. 6b with Fig. 15d.

Some insights into pressure-sensitivity effects on void growth patterns can be obtained from the deformed finite element meshes in Fig. 15. Comparing Fig. 15a with Fig. 15b for $\eta = 20$, we observe no qualitative difference between the damage patterns. The same can be said between Fig. 15c and Fig. 15d for $\eta = 100$. Thus pressure-sensitivity exert no significant effect on the deformed void pattern. This trend could be expected since pressure-sensitivity relates to hydrostatic stress effect on void expansion, and not on shape change.

6. Concluding remarks

This paper focuses on the void growth and interaction in polymeric solids. The proposed constitutive model captures several key characteristics of plastic flow in polymers, such as strain softening and rehardening, pressure-sensitivity and plastic dilatancy. The study consists of two parts.

In the first part, we study multiple void interaction and its effect on void growth and coalescence under constant stress triaxiality using a representative axisymmetric unit-cell. Our study suggests that certain aspects of damage and failure of glassy polymers can be interpreted in terms of its post-yield characteristics – strain softening and the rate of progressive rehardening. An extended strain softening regime enhances void growth rates with the voids becoming more oblate. Both contribute to reduced ductility (see Fig. 10a). When strain soften-

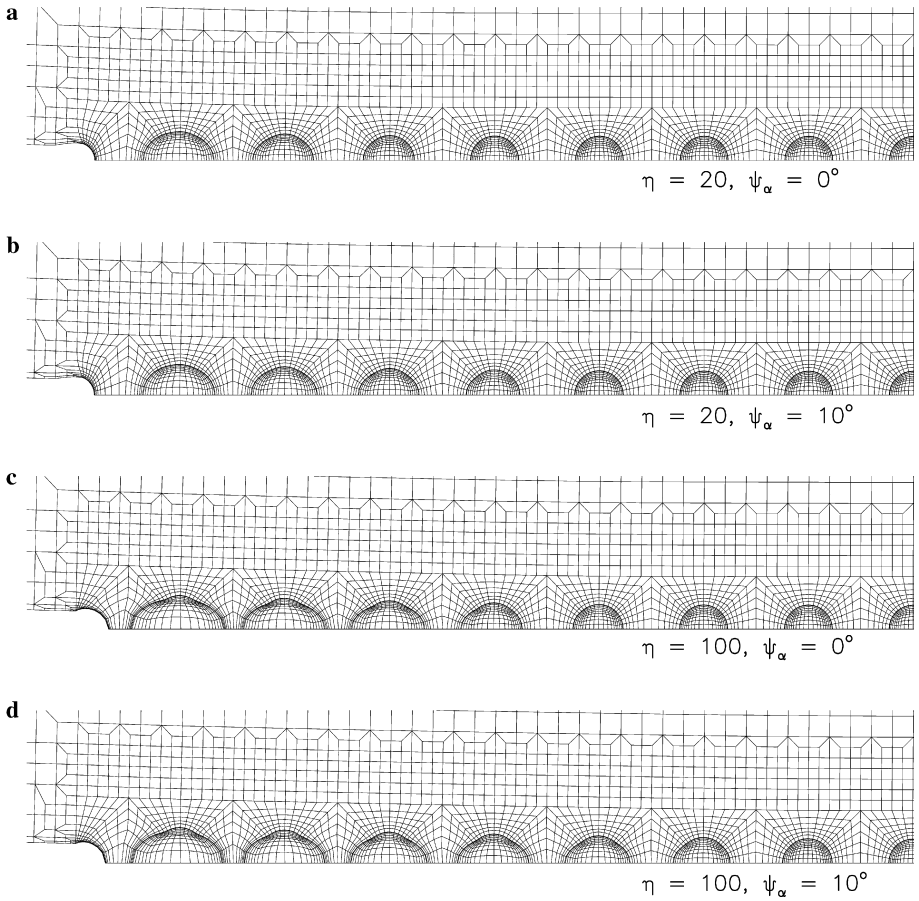

Fig. 15. Deformed meshes at $J/(\sigma_0 D) = 0.35$ for $f_0 = 0.05$: (a) $\eta = 20$, $\psi_\alpha = 0°$; (b) $\eta = 20$, $\psi_\alpha = 10°$; (c) $\eta = 100$, $\psi_\alpha = 0°$ and (d) $\eta = 100$, $\psi_\alpha = 10°$.

ing is followed by high rate of rehardening, the voids become more prolate. This reduces susceptibility to internal necking thereby enhancing ductility (see Fig. 10c). The effective strain at onset of coalescence is strongly affected by pressure-sensitivity and to a lesser extent by plastic dilatancy.

In the second part, we introduce a periodic planar array of discrete spherical voids ahead of a three-dimensional crack front. The small-scale yielding computational model is employed to study the softening–rehardening effects on the damage distribution and the evolution of void shapes near the crack front. Our studies indicate that the void interaction effects are greatly reduced in polymers exhibiting high rates of rehardening. On the other hand, voids in polymers with an extended strain softening regime behave differently. The voids become more oblate and a higher level of cooperative void growth and interaction is observed which results in a larger damage zone. This voiding pattern suggests that multiple void growth and interaction determine the fracture resistance of polymers. These tendencies are exacerbated by pressure sensitivity – see Figs. 14 and 15d.

Glassy polymers and polymer-rubber blends exhibit viscoplastic behavior. The phenomenological model proposed in this work can be extended to account for viscoplasticity. This is the subject for a future study. Such a study could facilitate direct comparison with more elaborate constitutive models by Boyce et al. (1988), Wu and Van der Giessen (1993) and Anand and Gurtin (2003).

Acknowledgement

The support of this work by the National University of Singapore (Grant No. R-265-000-136-112) is gratefully acknowledged.

Appendix A. Procedure for the multipoint constraint

The total work-rate $V\boldsymbol{\Sigma} : \dot{\mathbf{E}}$ of the axisymmetric cell can be cast into the dot product of a pair of two dimensional generalized force and displacement rate vectors $(P_i) = (2V\Sigma_\rho, V\Sigma_z)$ and $(\dot{Q}_i) = (\dot{E}_\rho, \dot{E}_z)$. That is to define

$$\mathbf{P} \cdot \dot{\mathbf{Q}} = V\boldsymbol{\Sigma} : \dot{\mathbf{E}} \tag{A.1}$$

where V is the current cell volume. The ratio of the current to initial cell volumes is $V/V_0 = \det \bar{\mathbf{F}} = \lambda_\rho^2 \lambda_z$. This newly defined work-rate $\mathbf{P} \cdot \dot{\mathbf{Q}}$ appears to be invariant under rotations in the vector plane. The symmetry group of (A.1) has a connected piece – the special orthogonal group SO(2). Let $\mathscr{R}$ denote this circle group, which has the matrix representation

$$\mathscr{R} = \begin{pmatrix} \cos\omega & -\sin\omega \\ \sin\omega & \cos\omega \end{pmatrix} \quad \text{with } 0 \leqslant \omega < 2\pi \tag{A.2}$$

where ω is the angle of rotation.

To construct the multipoint constraint equations, it is necessary to introduce one single isolated "ghost" node into the finite element model. Such an extra node has the ghost degrees of freedom q_1 and q_2 with the respective work-conjugate forces p_1 and p_2. Assume there exists work-rate equivalence between the ghost node and the entire axisymmetric cell:

$$\mathbf{p} \cdot \dot{\mathbf{q}} = \mathbf{P} \cdot \dot{\mathbf{Q}} \tag{A.3}$$

It follows immediately that:

$$\mathbf{p} = \mathscr{R}\mathbf{P}, \quad \dot{\mathbf{q}} = \mathscr{R}\dot{\mathbf{Q}} \tag{A.4}$$

Hence, the work-conjugate pair $(\mathbf{p}, \dot{\mathbf{q}})$ appears as an equivalent class of $(\mathbf{P}, \dot{\mathbf{Q}})$. Both are linked through the single parameter group SO(2). To uniquely determine the orthogonal rotation $\mathscr{R}$, we further specify the boundary condition on the ghost node: $p_1 = 0$. In other words, the nodal force conjugate to q_1 is set to zero. This solves the angle of rotation

$$\omega = \tan^{-1}(2\varphi) \tag{A.5}$$

where φ is the fixed stress ratio in (3.5). The orthogonal matrix (A.2) then becomes

$$\mathscr{R} = \begin{pmatrix} \frac{1}{\sqrt{1+4\varphi^2}} & -\frac{2\varphi}{\sqrt{1+4\varphi^2}} \\ \frac{2\varphi}{\sqrt{1+4\varphi^2}} & \frac{1}{\sqrt{1+4\varphi^2}} \end{pmatrix} \tag{A.6}$$

By the inverse transformation of $(A.4)_2$, the deformation rates $\dot{\mathbf{Q}}$ can be expressed in terms of the ghost displacement rates $\dot{\mathbf{q}}$. In component form,

$$\dot{E}_\rho = \frac{\dot{q}_1 + 2\varphi\dot{q}_2}{\sqrt{1+4\varphi^2}}, \quad \dot{E}_z = \frac{-2\varphi\dot{q}_1 + \dot{q}_2}{\sqrt{1+4\varphi^2}}. \tag{A.7}$$

Substituting (A.7) into (3.4) completes the construct of the multipoint constraint equations. The ghost node is coupled to the nodes on the outer surface of the unit cell.

Under the condition of $p_1 = 0$, the work-rate equivalence (A.3) implies

$$V\Sigma_z = \frac{p_2}{\sqrt{1+4\varphi^2}} \tag{A.8}$$

by use of (A.1) and (A.7). As a result, the macroscopic stress Σ_z can be computed directly from the reaction force p_2 of the ghost node.

Loading under a fixed stress ratio has been achieved by imposing the boundary condition $p_1 = 0$ and taking q_2 to be the proportional loading parameter. This procedure was implemented into ABAQUS (Hibbit et al., 2005) via the MPC user subroutine.

References

Anand, L., Gurtin, M.E., 2003. A theory of amorphous solids undergoing large deformations, with application to polymeric glasses. Int. J. Solids Struct. 40, 1465–1487.

Boyce, M., Parks, D., Argon, A.S., 1988. Large inelastic deformation of glassy polymers. Part I: Rate-dependent constitutive model. Mech. Mater. 7, 15–33.

Cheng, L., Guo, T.F., 2003. Vapor pressure assisted void growth and cracking of polymeric films and interfaces. Interf. Sci. 11, 277–290.

Chew, H.B., Guo, T.F., Cheng, L., 2005. Vapor pressure and residual stress effects on the failure of an adhesive film. Int. J. Solids Struct. 42, 4795–4810.

Chew, H.B., Guo, T.F., Cheng, L., 2006. Effects of pressure-sensitivity and plastic dilatancy on void growth and interaction. Int. J. Solids Struct. 43, 6380–6397.

Chowdhury, R.S., Narasimhan, R., 2000. A finite element analysis of stationary crack tip fields in a pressure sensitive constrained ductile layer. Int. J. Solids Struct. 37, 3079–3100.

Faleskog, J., Shih, C.F., 1997. Micromechanics of coalescence—I. Synergistic effects of elasticity, plastic yielding and multi-size scale voids. J. Mech. Phys. Solids 45, 21–50.

Guo, T.F., Cheng, L., 2002. Modeling vapor pressure effects on void rupture and crack growth resistance. Acta Mater. 50, 3487–3500.

Guo, T.F., Cheng, L., 2003. Vapor pressure and void size effects on failure of a constrained ductile film. J. Mech. Phys. Solids 51, 993–1014.

Guo, T.F., Yang, W., 1993. Crack tip profiles generated by anisotropic damage. Int. J. Damage Mech. 2, 364–384.

Guo, T.F., Faleskog, J., Shih, C.F., in preparation. Continuum modeling of a porous solid with pressure-sensitive and dilatant matrix.

Gurson, A.L., 1977. Continuum theory of ductile rupture by void nucleation and growth: Part I – Yield criteria and flow rules for porous ductile media. J. Eng. Mater. Technol. 99, 2–15.

G'Sell, C., Hiver, J.M., Dahoun, A., 2002. Experimental characterization of deformation damage in solid polymers under tension, and its interrelation with necking. Int. J. Solids Struct. 39, 3857–3872.

Hasan, O.A., Boyce, M.C., Li, X.S., Berko, S., 1993. An investigation of the yield and postyield behavior and corresponding structure of poly(methyl methacrylate). J. Polym. Sci.: Part B: Polym. Phys. 31, 185–197.

Hibbit, Karlsson & Sorensen Inc., Abaqus/Standard User's Manual, Version 6.5.1, vol. 1.

Huang, Y., Hutchinson, J.W., Tvergaard, V., 1991. Cavitation instabilities in elastic–plastic solids. J. Mech. Phys. Solids 39, 223–241.

Jeong, H.-Y., Li, X.-W., Yee, A.F., Pan, J., 1994. Slip lines in front of a notch tip in a pressure-sensitive material. Mech. Mater. 19, 29–38.

Kim, J., Gao, X., Srivatsan, T.S., 2003. Modeling of crack growth in ductile solids: a three-dimensional analysis. Int. J. Solids Struct. 40, 7357–7374.

Kim, G.-M., Michler, G.H., Gahleitner, M., Fiebig, J., 1996. Relationship between morphology and micromechanical toughening mechanisms in modified polypropylenes. J. Appl. Polym. Sci. 60, 1391–1403.

Koplik, J., Needleman, A., 1988. Void growth and coalescence in porous plastic solids. Int. J. Solids Struct. 24, 835–853.

Kramer, J.K., Berger, L.L., 1990. Fundamental processes of craze growth and fracture. Adv. Polym. Sci. (91/92), 1–68.

Moran, B., Shih, C.F., 1987. A general treatment of crack tip contour integrals. Int. J. Fracture 35, 363–371.

Perrin, G., Leblond, J.-B., 2000. Accelerated void growth in porous ductile solids containing two populations of cavities. Int. J. Plasticity 16, 91–120.

Quinson, R., Perez, J., Rink, M., Pavan, A., 1997. Yield criteria for amorphous glassy polymers. J. Mater. Sci. 32, 1371–1379.

Subramanya, H.Y., Viswanath, S., Narasimhan, R., 2006. A three-dimensional numerical study of mode I crack tip fields in pressure sensitive plastic solids. Int. J. Solids Struct.. doi:10.1016/j.ijsolstr.2006.08.003.

Steenbrink, A.C., Van der Giessen, E., 1997a. Void growth in glassy polymers: effect of yield properties on hydrostatic expansion. Int. J. Damage Mech. 6, 317–330.

Steenbrink, A.C., Van der Giessen, E., 1997b. Void growth in glassy polymers. J. Mech. Phys. Solids 45, 405–437.

Tvergaard, V., 1998. Interaction of very small voids with larger voids. Int. J. Solids Struct. 35, 3989–4000.

Tvergaard, V., 1999. Effect of large elastic strains on cavitation instability predictions for elastic–plastic solids. Int. J. Solids Struct. 36, 5453–5466.

Tvergaard, V., Hutchinson, J.W., 2002. Two mechanisms of ductile fracture: void by void growth versus multiple void interaction. Int. J. Solids Struct. 39, 3581–3597.

Tvergaard, V., Needleman, A., 1984. Analysis of cup-cone facture in a round tensile bar. Acta Metall. 32, 157–169.

Utz, M., Peng, Q., Nandagopal, M., 2004. Athermal simulation of plastic deformation in amorphous solids at constant pressure. J. Polymer Sci.: Part B: Polym. Phys. 42, 2057–2065.

Wu, P.D., Van der Giessen, E., 1993. On improved network models for rubber elasticity and their applications to orientation hardening of glassy polymers. J. Mech. Phys. Solids 41, 427–456.

Wright, W.J., Hufnagel, T.C., Nix, W.D., 2003. Free volume coalescence and void formation in shear bands in metallic glass. J. Appl. Phys. 93 (3), 1432–1437.

Xia, L., Shih, C.F., 1995a. Ductile crack growth – I. A numerical study using computational cells with microstructurally-based length scales. J. Mech. Phys. Solids 43, 233–259.

Xia, L., Shih, C.F., 1995b. Ductile crack growth – II. Void nucleation and geometry effects on macroscopic fracture behavior. J. Mech. Phys. Solids 43, 1953–1981.

Xia, L., Shih, C.F., Hutchinson, J.W., 1995. A computational approach to ductile crack growth under large scale yielding conditions. J. Mech. Phys. Solids 43, 389–413.

Yang, W., Guo, T.F., Fu, Z.L., 1993. Crack tip superblunting: experiment, theory and numerical simulation. Acta Mech. Sinica 9, 131–141.